PROCEEDINGS OF SCIENCE

ATLAS Results on Hard and Electromagnetic Probes in Heavy-Ion Collisions

Petr Balek* **on behalf of the ATLAS collaboration**

AGH University of Krakow,
al. Adama Mickiewicza 30, 30-059 Kraków, Poland

E-mail: petr.balek@cern.ch

The ATLAS experiment at the Large Hadron Collider (LHC) encompasses a wide-ranging physics program that includes a variety of collision systems and energies. These proceedings provide an overview of the recent ATLAS measurements regarding heavy ion collisions and related topics. The data utilized in the presented results were recorded during LHC Run 2 (2015–2018). The measurements can help to understand various physics phenomena from hard scatterings to soft processes; from large systems through small systems and photon-induced interactions; and from precision measurements to searches for physics beyond the Standard Model.

HardProbes2023
26-31 March 2023
Aschaffenburg, Germany

*Speaker

PoS(HardProbes2023)002

1. Introduction

The heavy ion program of the ATLAS experiment at the Large Hadron Collider (LHC) [1] is rich and encompasses systems of different sizes. In the large collision systems, Pb+Pb and Xe+Xe, it explores the phenomenon of jet quenching in quark-gluon plasma (QGP) and its dependency on the sub-structure, color charge, or quark flavour of jets; this is reviewed in Sec. 2. In the small collision systems, pp and p+Pb, the program focuses on the origin of collective effects, formation of quarkonia, and the mechanism behind the jet modification; this is discussed in Sec. 3. Furthermore, photon–photon (γ+γ) and photonuclear collisions are studied by using intense photon fluxes accompanying Pb+Pb collisions. It leads to the measurements of the γ+γ-fusion cross sections, nuclear parton distribution functions (nPDFs), and searches for physics beyond the Standard Model; this is described in Sec. 4.

2. Large Systems

The imbalance of the di-jet system is quantized with the transverse momenta of the jets as $x_J = p_{\mathrm{T}}^{subleading}/p_{\mathrm{T}}^{leading}$. The measurement in Pb+Pb collisions at $\sqrt{s_{\mathrm{NN}}} = 5.02$ TeV [2] shows an emergence of a peak structure at $x_J \approx 0.6$. Only after examination the absolutely normalized results, shown in Fig. 1, it becomes apparent that the peak is a consequence of large suppression of di-jets with $x_J \gtrsim 0.8$ and relatively lower suppression of di-jets with smaller x_J. The di-jet imbalance in Xe+Xe collisions [3] is consistent with the one obtained in Pb+Pb collisions when accounting for the same energy in the forward calorimeter and correcting for higher center-of-mass energy in Xe+Xe collisions.

The dependence of the partonic energy loss on jet substructure is studied across multiple lengths. At small lengths, the constituents of anti-k$_t$ ($R = 0.4$) jets [4] are re-clustered using Cambridge–Aachen algorithm. Subsequently, a soft-drop procedure is used to identify the first hard splitting within the jet. The nuclear modification factor, R_{AA}, is studied with respect to the angle between these two sub-jets, r_g [5]. For fixed r_g, R_{AA} exhibits a relatively weak dependence on jet p_{T}, as illustrated in Fig. 2. Because the inclusive R_{AA} tends to increase as p_{T} increases, it means that the jets with smaller r_g are more prevalent among high-p_{T} jets.

At larger lengths, large anti-k$_t$ ($R = 1.0$) jets are clustered from smaller anti-k$_t$ ($R = 0.2$) jets [6]. Here, the k$_t$ jet algorithm is utilized to identify the hardest splitting. Figure 3 shows the

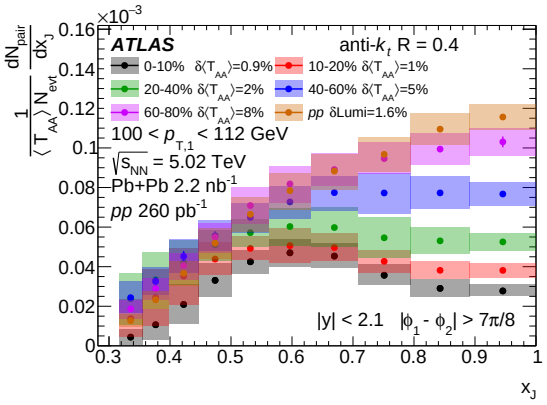

Figure 1: Absolutely normalized x_J distributions in pp collisions and for five centrality intervals in Pb+Pb collisions [2]. Statistical uncertainties are shown as vertical bars (often smaller than the markers); systematic uncertainties are shown as boxes. Fully correlated uncertainties due to the pp luminosity and $\langle T_{\mathrm{AA}} \rangle$ are listed in legends.

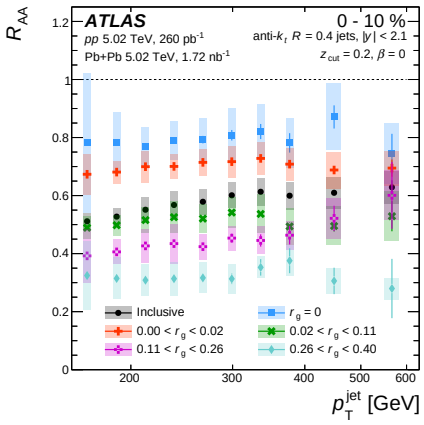

Figure 2: Nuclear modification factor, R_{AA}, as a function of jet p_{T} for soft-drop groomed jets in four intervals of r_g [5]. Groomed jet R_{AA} values are compared with R_{AA} values of jets without significant splitting ($r_g = 0$) and inclusive jets (without grooming). Vertical bars represent statistical uncertainties, whereas boxes represent bin-wise correlated systematic uncertainties. Fully correlated uncertainties due to the pp luminosity (1.6%) and $\langle T_{\mathrm{AA}} \rangle$ are not shown. ←

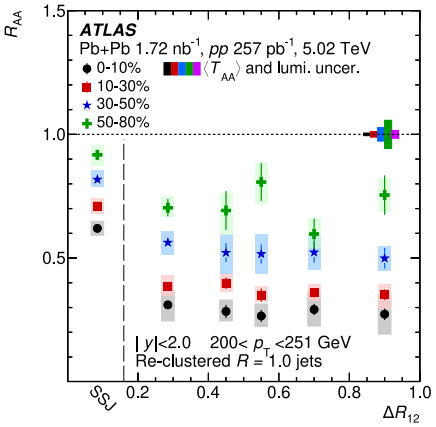

Figure 3: Nuclear modification factor, R_{AA}, for $R = 1.0$ re-clustered jets as function of ΔR_{12} in four centrality intervals [6]. The label "SSJ" on the x-axis identifies the single sub-jet configuration. The vertical bars indicate statistical uncertainties, the shaded boxes indicate systematic uncertainties. The fully correlated uncertainties due to the pp luminosity and $\langle T_{\mathrm{AA}} \rangle$ are represented by boxes at unity. ➔

R_{AA} dependence on the angular separation of the two sub-jets before the final clustering step of $R = 1.0$ jet. There is a discernible distinction between scenarios where only a single sub-jet is found ("SSJ"), indication of coherent parton radiation, and cases where at least two sub-jets are found ($\Delta R_{12} \gtrsim 0.2$) and partons radiate decoherently. Due to limitations in experimental resolution, it is not possible to measure the region where these two effects would overlap, namely $\Delta R_{12} \lesssim 0.2$.

Even larger lengths can be probed in photon + multi-jet events [7]. The di-jet system is compared to the recoiled photon. The separation between the two jets is denoted as ΔR_{JJ}. Figure 4 shows that the energy loss is less pronounced for small values of ΔR_{JJ} and more pronounced for large values.

The dependence of the nuclear modification factor R_{AA} on the quark flavour is studied in Ref. [8]. To reconstruct jets, the anti-k$_t$ ($R = 0.2$) algorithm is used and possible b-jets are identified through the presence of a muon. The energy of b-jets is corrected to account also for missing neutrinos. As seen in Fig. 5, the suppression of b-jets is comparable to that of inclusive jets in the peripheral Pb+Pb collisions. In the central collisions, b-jets experience about 20% less suppression.

The production of bottomonia states, Υ(1S), Υ(2S), and Υ(3S), is also modified in Pb+Pb collisions [12]. The measurement uses $\mu\mu$ decay channel and Fig. 6 presents the relevant nuclear modification factor measurement. With increasing centrality, and thus increasing $\langle N_{\mathrm{part}} \rangle$, the production of Υ states becomes more suppressed. This suppression can be attributed to a combination of energy loss and Debye screening.

Production of charged hadrons is suppressed in heavy ion collisions as well [14]; this is shown in Fig. 7. In both Pb+Pb and Xe+Xe collisions the suppression is stronger with higher values of

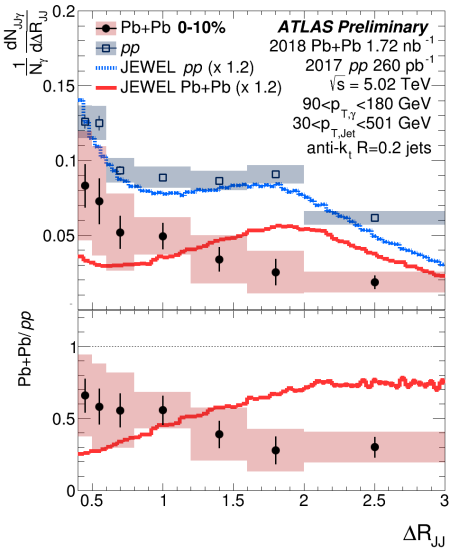

Figure 4: ΔR_{JJ} in photon plus multi-jet events in Pb+Pb collisions in 0-10% centrality interval and in *pp* collisions [7]. Statistical and systematic uncertainties are plotted as vertical bars and shaded boxes, respectively. Also shown are the predictions of the JEWEL model for *pp* events and Pb+Pb events, scaled by a factor of 1.2. The ratio of the Pb+Pb to *pp* distributions is shown in the bottom panel. ←

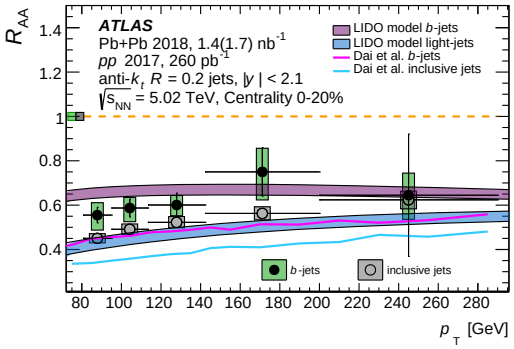

Figure 5: R_{AA} for b-jets for the centrality 0-20% compared with the inclusive jet R_{AA} [8]. Statistical and systematic uncertainties are plotted as vertical bars and shaded boxes, respectively. The boxes at unity represent the uncertainties from $\langle T_{\mathrm{AA}} \rangle$ and *pp* luminosity. Both measurements are compared to theoretical calculations [9–11]. ➔

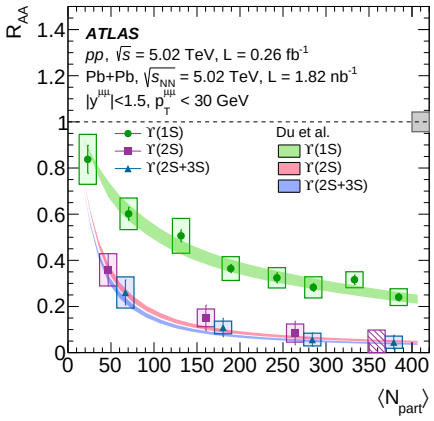

Figure 6: Nuclear modification factor for ϒ(1S), ϒ(2S), and ϒ(2S+3S) as a function of $\langle N_{\mathrm{part}} \rangle$ [12]. Vertical bars indicate the statistical uncertainties and boxes represent the systematic uncertainties. The gray box around unity corresponds to the global systematic uncertainty. The results are compared with theory calculation from Ref. [13]. ←

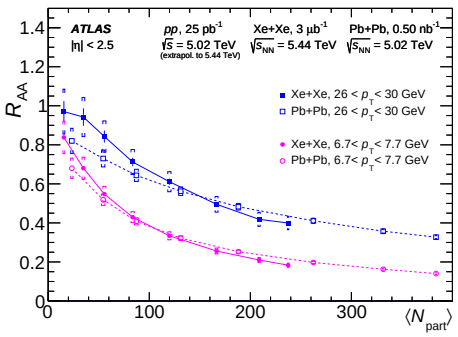

Figure 7: Nuclear modification factor for charged particles as a function of $\langle N_{\mathrm{part}} \rangle$ for selected ranges of p_{T} measured in Pb+Pb and Xe+Xe collisions [14]. Systematic uncertainties are shown with brackets; statistical uncertainties are shown with vertical lines. The horizontal widths of the brackets represent systematic uncertainties on $\langle N_{\mathrm{part}} \rangle$. ➔

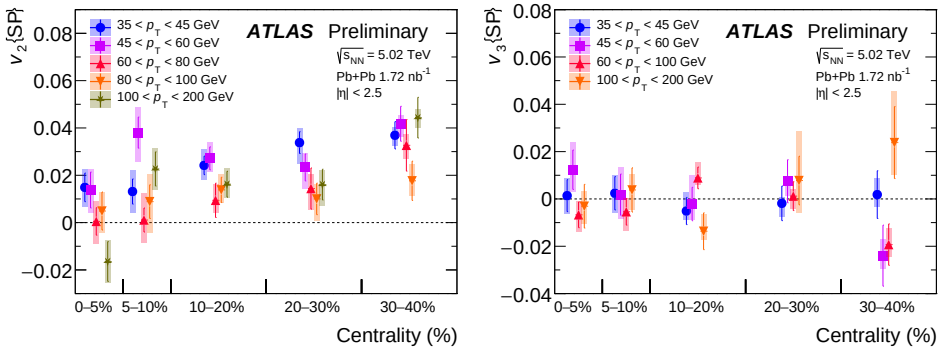

Figure 8: The v_2 (left) and v_3 (right) values as a function of centrality for charged particles in selected p_T ranges [15]. The statistical uncertainties are shown as vertical bars, the systematic uncertainties with boxes.

$\langle N_{\text{part}} \rangle$. For a fixed $\langle N_{\text{part}} \rangle$, the two collision systems do not yield the same level of suppression.

Understanding azimuthal anisotropy in heavy ion collisions is also crucial for comprehending QGP. Figure 8 shows measurement of elliptic and triangular flows, up to high-p_T [15]. The scalar product method [16] is used to eliminate contributions arising from jets. When compared to similar observables measured for jets [17], the values of v_2 are positive in both cases, even at high p_T. However, values of v_3 are consistent with zero, whereas for jets, the positive v_3 values are observed. A possible explanation lies in a different η ranges of the results.

3. Small Systems

In contrast to Pb+Pb or Xe+Xe collisions, there is no jet quenching expected in p+Pb collisions. Nevertheless, there might be some less obvious modifications of jet kinematics present. Figure 9 compares the tracks produced per jet in p+Pb and pp collisions [18]. On the away side, their ratios are consistent with unity, while on the near side, there is an enhancement of approximately 5%. This is consistent with a theoretical prediction [19, 20] that does not include final-state effects producing collectivity or jet quenching.

A detailed study of di-jet production in p+Pb collisions is presented in Fig. 10 in different ranges of di-jet boost, y_b, and the half of rapidity separation, y^* [21]. The central-to-peripheral ratio, R_{CP}, reveals a suppression in the di-jet yield measured in central p+Pb collisions compared to peripheral ones. For the momentum fraction of the proton, x_p, the observed suppression follows the same trend in almost all (y_b, y^*) ranges. No such trend is present for the Pb momentum fraction, x_{Pb}.

While the presence of the azimuthal correlations is widely acknowledged in heavy ion collisions, their presence in pp collisions was not expected. To shed more light onto this phenomenon, Fig. 11 shows a measurement of v_2 in pp collisions for two particle–particle selections [22]. The correlations are evaluated using either only particles from the underlying event ("h^{UE}-h^{UE}") or by pairing a particle from the underlying event with a particle from a jet ("h^{UE}-h^{J}"). While the first pairing yields a significant non-zero v_2, the second one yields v_2 consistent with zero. This suggests a "factorization" between hard-scattering processes and the physics responsible for the 'ridge' effect.

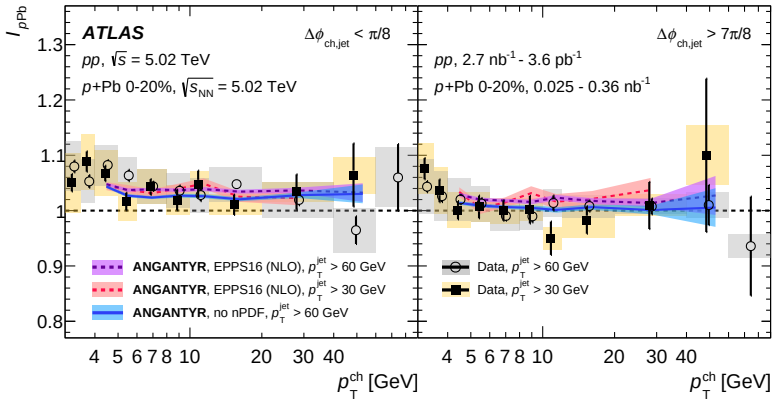

Figure 9: The ratio of per-jet charged-particle yields, I_{pPb}, on the near-side and away-side between p+Pb and pp collisions for the 0-20% centrality [18]. Particles correlated with a jet above 30 GeV and 60 GeV are shown. Statistical uncertainties are shown as vertical bars; systematic uncertainties as filled boxes. Also shown are calculations from the Angantyr model [19] with (EPPS16 (NLO)) and without (no PDF) nuclear-modified parton distribution functions [20]. The colored bands of Angantyr represent statistical uncertainties only.

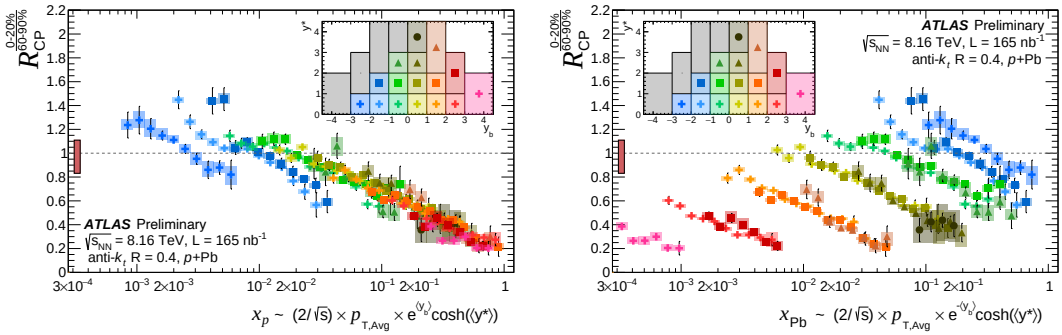

Figure 10: R_{CP} as a function of approximated x_p and x_{Pb} [21]. An inlay legend shows the corresponding markers of the (y_b, y^*) ranges. The positive y_b corresponds to the proton-going direction. Boxes represent the total systematic uncertainty; the vertical lines represent the statistical uncertainty. The uncertainty on the $\langle T_{\mathrm{AB}} \rangle$ is shown at unity. Four (y_b, y^*) ranges, denoted by a gray color, were dropped from the analysis as the presence of jets in these intervals may bias the centrality determination.

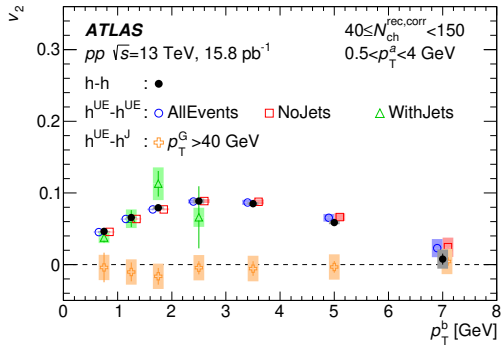

Figure 11: The p_{T} dependence of v_2 for charged particles in pp collisions [22]. Jets with $p_{\mathrm{T}} > 15$ GeV are used to classify the NoJet and WithJet samples. The data-points for the "h-h" sample are drawn at the nominal values while the other data-points may be slightly shifted for clarity. The vertical bars and boxes correspond to statistical and systematic uncertainties, respectively.

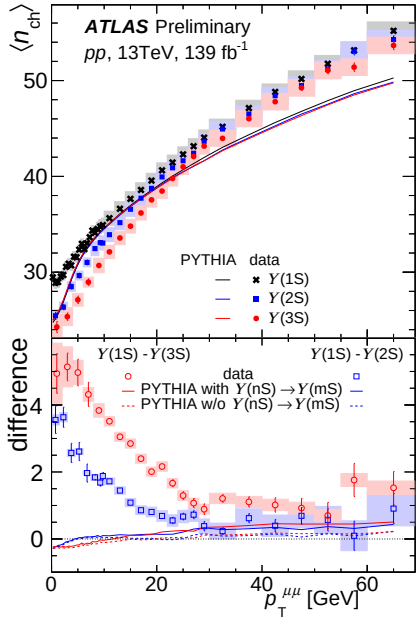

Figure 12: The mean number of charged particles with $0.5 < p_{\mathrm{T}} < 10\,\mathrm{GeV}$ and $|\eta| < 2.5$ in events with Υ(nS) mesons (top) and difference of this quantity between the excited and ground Υ(nS) state (bottom) [23]. Pythia8 predictions with (solid) and without (dashed) $\Upsilon(\mathrm{nS}) \to \Upsilon(\mathrm{mS})$ contributions are also shown. Statistical uncertainties are shown with vertical bars, boxes are systematic uncertainties.

Measurement of Υ production in high-statistics pp collisions is presented in Fig. 12, featuring precise subtraction of pile-up events and underlying-event contributions [23]. It shows that as the collision multiplicity increases, the likelihood of observing Υ(2S) and Υ(3S) states diminishes compared to the ground state Υ(1S). This suggests a possible correlation between the underlying event and the hard scattering process.

4. Ultra-Peripheral Collisions

The nature of heavy ion collisions provides an opportunity to also study the electromagnetic interaction between nuclei. To gain a deeper understanding of the photon flux in such collisions, exclusive di-lepton production is studied [24, 25]. The cross sections of $\gamma\gamma \to e^-e^+$ and $\gamma\gamma \to \mu^-\mu^+$ are shown on Figs. 13 and 14, respectively. The measurements are compared to STARlight [26] and SuperChic 3 [27] event generators.

Additionally, the exclusive di-lepton production can be also utilized in searches for physics beyond the Standard Model. A measurement of di-τ production can set constraints on the anomalous magnetic moment, a_τ [28]. The extracted limits on a_τ are shown in Fig. 15. They are consistent with the Standard Model prediction and have comparable precision as reported by DELPHI collaboration at LEP [29].

Di-leptons produced via $\gamma\gamma$ scattering are also present even when hadronic hard-scattering process has occurred. A study focusing on di-muons produced in non-ultra-peripheral collisions is presented in Ref. [32] and shown in Fig. 16. With increasing centrality, a broadening of the di-muon acoplanarity, α, distribution is observed along with a depletion at low α. The same features are also seen in theoretical calculations [33, 34].

A measurement of di-jet photoproduction in ultra-peripheral Pb+Pb collisions is shown in Fig. 17 [35]. The cross section is measured differentially with respect to the scalar sum of the

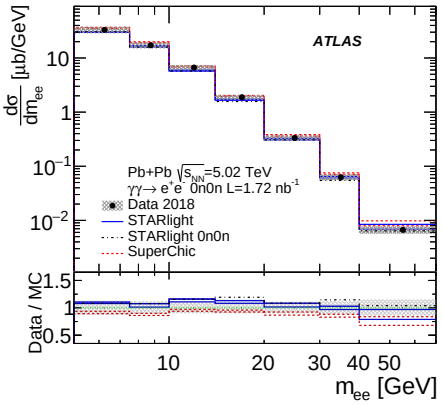

Figure 13: Differential cross sections measured inclusively in ZDC categories for exclusive di-electron production as a function of m_{ee} [24]. The data are compared to the predictions from Starlight [26] and SuperChic 3 [27]. The bottom panel present the ratios of data to the predictions. The shaded area represents the total uncertainty of the data, excluding luminosity uncertainty. ←

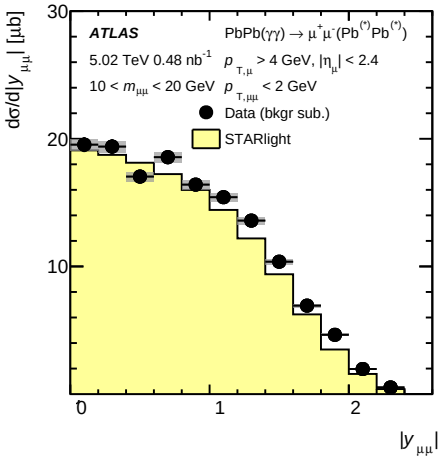

Figure 14: Differential cross sections shown as a function of $|y_{\mu\mu}|$ compared with cross sections from STARlight [25, 26]. Statistical uncertainties are shown as error bars while total systematic uncertainties are shown as gray boxes. ➔

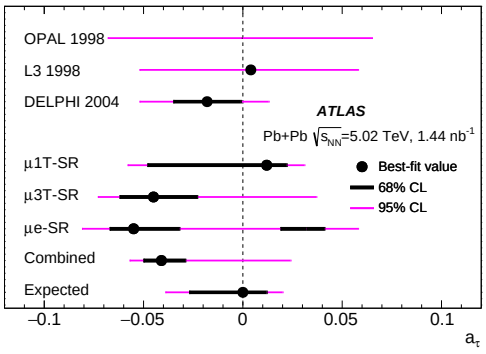

Figure 15: Measurements of a_τ from fits to individual signal regions and from the combined fit [28] compared with existing measurements from the OPAL [30], L3 [31] and DELPHI [29] experiments at LEP. A point denotes the best-fit a_τ value for each measurement if available, while thick black (thin magenta) lines show 68% CL (95% CL) intervals. ←

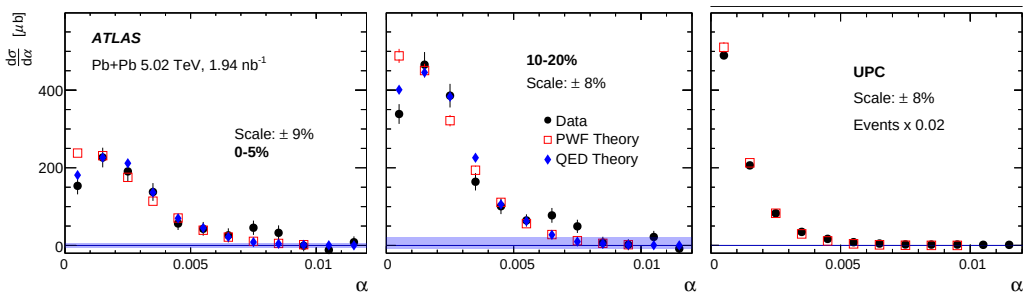

Figure 16: Differential cross sections as a function of α for $\gamma\gamma \to \mu\mu$ pairs passing the Fid-α selection in selected centrality intervals [32]. Vertical bars indicate combined statistical and systematic uncertainties, excluding the background subtraction uncertainties, which are indicated by a shaded band at zero, and overall normalization uncertainties, which are quoted on each panel as “Scale". Also shown are the results of ’QED’ [33] and ’PWF’ [34] theoretical calculations.

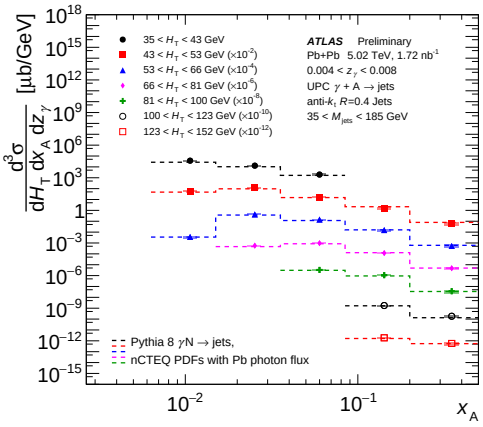

Figure 17: Triple-differential cross sections for di-jet photoproduction as a function of x_A for different bins of H_T [35]. Systematic uncertainties are shown as shaded boxes, while statistical uncertainties shown as vertical lines are usually smaller than the size of the markers. A comparison is shown to the cross sections computed using PYTHIA 8 with nCTEQ PDFs, a photon flux from Starlight, and a z_γ-dependent breakup fraction.

jet transverse momenta, H_T, the nuclear parton momentum fraction, x_A, and the photon parton momentum fraction, z_γ. This detailed measurement will help to constrain nuclear PDFs.

5. Summary

In the 11th International Conference on Hard and Electromagnetic Probes of High-Energy Nuclear Collisions, the ATLAS experiment presented a diverse range of new results, utilizing data recorded during Run 2 of the LHC. This includes the exploration of the jet substructure and interaction between partons and QGP in large systems, investigation of QGP-like behaviour in small systems, and using ions as a source of photons of high intensity for searches of physics beyond the Standard Model.

Acknowledgements

This work was partly supported by the National Science Centre of Poland under grant number UMO-2020/37/B/ST2/01043 and by PL-GRID infrastructure.

References

[1] ATLAS Collaboration. *JINST* **3** (2008) S08003.

[2] ATLAS Collaboration. *Phys. Rev. C* **107** (2023) 054908 [2205.00682].

[3] ATLAS Collaboration. [2302.03967].

[4] M. Cacciari et al. *JHEP* **04** (2008) 063 [0802.1189].

[5] ATLAS Collaboration. *Phys. Rev. C* **107** (2023) 054909 [2211.11470].

[6] ATLAS Collaboration. [2301.05606].

[7] ATLAS Collaboration. *ATLAS-CONF-2023-008*.

[8] ATLAS Collaboration. *Eur. Phys. J. C* **83** (2023) 438 [2204.13530].

[9] W. Ke et al. *Phys. Rev. C* **98** (2018) 064901 [1806.08848].

[10] W. Dai et al. *Chin. Phys. C* **44** (2020) 104105 [1806.06332].

[11] W. Ke et al. *Phys. Rev. C* **100** (2019) 064911 [1810.08177].

[12] ATLAS Collaboration. *Phys. Rev. C* **107** (2023) 054912 [2205.03042].

[13] X. Du et al. *Phys. Rev. C* **96** (2017) 054901 [1706.08670].

[14] ATLAS Collaboration. *JHEP* **07** (2023) 074 [2211.15257].

[15] ATLAS Collaboration. *ATLAS-CONF-2023-007*.

[16] STAR Collaboration. *Phys. Rev. C* **66** (2002) 034904 [nucl-ex/0206001].

[17] ATLAS Collaboration. *Phys. Rev. C* **105** (2022) 064903 [2111.06606].

[18] ATLAS Collaboration. [2206.01138].

[19] C. Bierlich et al. *JHEP* **10** (2018) 134 [1806.10820].

[20] K. J. Eskola et al. *Eur. Phys. J. C* **77** (2017) 163 [1612.05741].

[21] ATLAS Collaboration. *ATLAS-CONF-2023-011*.

[22] ATLAS Collaboration. [2303.17357].

[23] ATLAS Collaboration. *ATLAS-CONF-2022-023*.

[24] ATLAS Collaboration. *JHEP* **06** (2023) 182 [2207.12781].

[25] ATLAS Collaboration. *Phys. Rev. C* **104** (2021) 024906 [2011.12211].

[26] S. R. Klein et al. *Comput. Phys. Commun.* **212** (2017) 258 [1607.03838].

[27] L. A. Harland-Lang et al. *Eur. Phys. J. C* **80** (2020) 925 [2007.12704].

[28] ATLAS Collaboration. [2204.13478].

[29] DELPHI Collaboration. *Eur. Phys. J. C* **35** (2004) 159 [hep-ex/0406010].

[30] OPAL Collaboration. *Phys. Lett. B* **431** (1998) 188 [hep-ex/9803020].

[31] L3 Collaboration. *Phys. Lett. B* **434** (1998) 169.

[32] ATLAS Collaboration. *Phys. Rev. C* **107** (2023) 054907 [2206.12594].

[33] W. Zha et al. *Phys. Lett. B* **800** (2020) 135089 [1812.02820].

[34] S. Klein et al. *Phys. Rev. D* **102** (2020) 094013 [2003.02947].

[35] ATLAS Collaboration. *ATLAS-CONF-2022-021*.